ACS APPLIED MATERIALS & INTERFACES

Research Article

www.acsami.org

Bipolar Electric-Field Enhanced Trapping and Detrapping of Mobile Donors in $BiFeO_3$ Memristors

Tiangui You,*[,†] Nan Du,[†] Stefan Slesazeck,[‡] Thomas Mikolajick,[‡,§] Guodong Li,[∥] Danilo Bürger,[†] Ilona Skorupa,[⊥] Hartmut Stöcker,[#] Barbara Abendroth,[#] Andreas Beyer,[△] Kerstin Volz,[△] Oliver G. Schmidt,[†,∥] and Heidemarie Schmidt*[,†]

[†]Material Systems for Nanoelectronics, Technische Universität Chemnitz, Chemnitz 09126, Germany

[‡]NaMLab gGmbH, Dresden 01187, Germany

[§]Institute of Semiconductors and Microsystems, Technische Universität Dresden, Dresden 01187, Germany

[∥]Institute for Integrative Nanosciences, IFW Dresden, Dresden 01069, Germany

[⊥]HZDR Innovation GmbH, Dresden 01328, Germany

[#]Institut für Experimentelle Physik, Technische Universität Bergakademie Freiberg, 09596 Freiberg, Germany

[△]Materials Science Center and Faculty of Physics, Philipps-Universität Marburg, Marburg 35032, Germany

Supporting Information

ABSTRACT: Pulsed laser deposited Au-BFO-Pt/Ti/Sapphire MIM structures offer excellent bipolar resistive switching performance, including electroforming free, long retention time at 358 K, and highly stable endurance. Here we develop a model on modifiable Schottky barrier heights and elucidate the physical origin underlying resistive switching in $BiFeO_3$ memristors containing mobile oxygen vacancies. Increased switching speed is possible by applying a large amplitude writing pulse as the resistive switching is tunable by both the amplitude and length of the writing pulse. The local resistive switching has been investigated by conductive atomic force microscopy and exhibits the capability of down-scaling the resistive switching cell to the grain size.

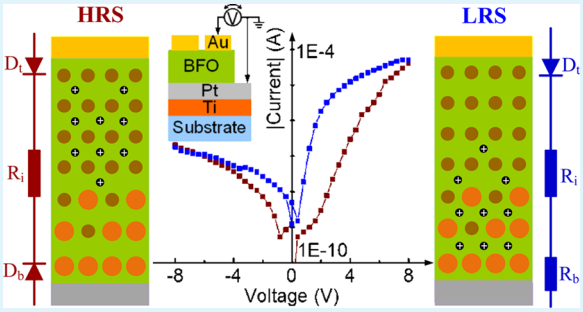

KEYWORDS: *bipolar resistive switching, mobile oxygen vacancy, modifiable rectification properties, Ti diffusion, reliability, $BiFeO_3$ thin films*

1. INTRODUCTION

As the conventional semiconductor memory technologies are expected to approach their physical limits in the near future, nonvolatile memories with high-density, high-speed, and low-power that can replace flash memories and dynamic random access memories (DRAM) are required.[1,2] Reversible resistive switching devices, known as "ReRAM" or "Memristors", are considered as one of the most promising candidates for the next generation of highly scalable nonvolatile memories.[3,4] Additionally, these simple structures consisting only of a metal−semiconductor (or insulator)−metal sandwich stack (MIM) have the potential to be used in reconfigurable nonvolatile logics,[2,5,6] cognitive computing[7,8] and data encryption.[9] Resistive switching characteristics with different switching behaviors, including bipolar resistive switching,[2,4−6] and unipolar resistive switching,[10,11] have been investigated in many materials, e.g., binary transition metal oxides,[2,4−6,10,11] ternary and multicomponent perovskite-type oxides,[12,13] and some other materials.[5,14] A number of chemical and physical models have also been proposed to explain the resistive switching behaviors, including formation and rupture of nanoscale conduction paths within insulator layers by either thermochemical processes or valence change,[3,5,11] modification of the Schottky barrier height[12,13,15,16] and electron trapping/detrapping.[17] It is possible that several different mechanisms may coexist, and different mechanisms could be dominant in different material systems.

$BiFeO_3$ (BFO) is a well-known multiferroic material and has attracted considerable attention because of its fascinating physical properties, e.g., its photovoltaic effect,[16,18] which offers the potential to develop radical new concepts for resistive switching devices. In recent years, the resistive switching behavior has been also observed in BFO thin films in MIM structures.[12,16,19−25] Most of the observed resistive switching behavior is attributed to the switching of ferroelectric polarization[12,19−22] or the migration of oxygen vacancies[16,23−25] under applied electric field. However, the ferroelectric polarization fatigue would limit the endurance[12,22] and the

Received: July 23, 2014
Accepted: November 4, 2014
Published: November 4, 2014

migration of oxygen vacancies under low electric field with longer time constant[26] might cause the resistive switching degradation by the small reading bias which limits the retention time. Therefore, the challenges still remain to achieve excellent resistive switching performance, including long retention time, good endurance, fast switching activity, and large storage window.[27,28] In this work, we present an Au-BFO-Pt/Ti/Sapphire MIM structure with excellent bipolar resistive switching, which is caused by the modulation of the Schottky barrier forming at the BFO-Pt bottom interface by the bias-driven forward−backward migration of mobile oxygen vacancies. Stable endurance and retention are obtained by the enhanced local electric field and the trapping of mobile oxygen vacancies. The resistive switching is tunable by the amplitude and length of the writing bias pulse and it is possible to scale down the size of resistive switching cells to the grain size.

2. EXPERIMENTAL SECTION

Polycrystalline BFO thin films with *R*3*c* space group (see Figure S1 in the Supporting Information) were deposited by pulsed laser deposition (PLD) on Pt/Ti/Sapphire substrates. The nominal laser energy density, laser repetition rate, oxygen ambient pressure, and growth temperature are 2.6 J/cm^2, 10 Hz, 0.013 mbar, and 650 °C, respectively. After the PLD process, the BFO thin films were in situ annealed at 390 °C with the oxygen ambient pressure of 200 mbar for 60 min. The nominal thickness of BFO thin films is 600 nm. Following the deposition, circular Au top contacts with an area of 0.045 mm^2 and a thickness of 30 nm were fabricated by DC magnetron sputtering at room temperature using a metal shadow mask. The schematic sketch of the Au-BFO-Pt/Ti/Sapphire MIM structure is displayed in the inset of Figure 1b.

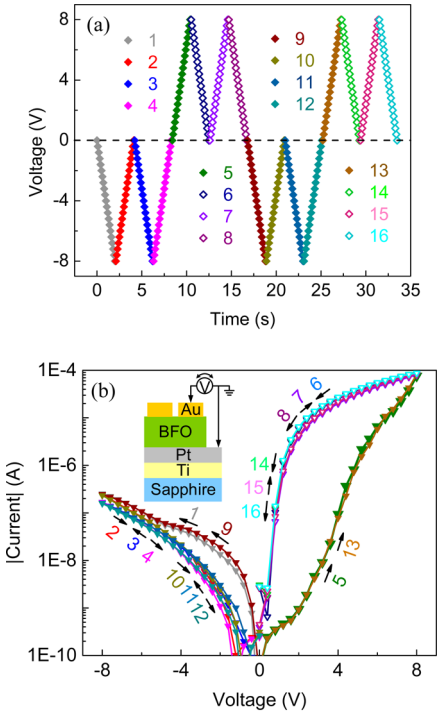

Figure 1. (a) Sequence of applied ramping voltages; (b) current−voltage (*I*−*V*) curves of the Au-BFO-Pt/Ti/Sapphire MIM structure. The numbers 1−16 label successive ramping voltages and corresponding current branches on a logarithmic scale, and the arrows indicate the scanning direction of the applied ramping voltages. The inset in (b) exhibits the schematic setup for the electric measurements.

The X-ray diffraction measurement was characterized by a Bruker D8 Advance diffractometer with parallel beam geometry using Cu Kα radiation at a fixed angle of incidence of 7°. The electric measurements were carried out using a Keithley 2400 source meter. The high-angle annular dark-field scanning transmission electron microscopy (HAADF-STEM) and the energy-dispersive X-ray spectroscopy (EDX) measurements were performed with a JEOL JEM 2200FS, double Cs-corrected scanning transmission electron microscope. The conductive AFM measurements were carried out with an Agilent Technologies 5420 scanning probe microscope.

3. RESULTS AND DISCUSSION

3.1. Resistive Switching Characteristics. The current−voltage (*I*−*V*) measurements were carried out with a Keithley 2400 source meter. The schematic sketch of the electrical measurement configuration is indicated by the inset in Figure 1b, in which the bias voltage was applied between Au top electrode and Pt bottom electrode. The Pt bottom electrode was grounded. Figure 1a shows a sequence of ramping voltages, namely two negative triangular voltage sweeps followed by two positive triangular voltage sweeps. The voltage step is 0.4 V with the step time of 0.1 s. Figure 1b shows the obtained *I*−*V* curves from the Au-BFO-Pt/Ti/Sapphire MIM structure. The numbers 1−16 label successive ramping voltages and the corresponding current branches in the *I*−*V* curves, and the arrows indicate the scanning direction of the applied ramping voltages. A distinct resistive switching behavior is observed at the positive bias range. After a positive ramping voltage (branch 5 or 13), the MIM structure exhibits a low resistance state (LRS) in the following positive ramping bias (branch 6, 7, 8 or 14, 15, 16). While the MIM structure shows high resistance state (HRS) in negative ramping bias. This suggests the nonvolatile resistive switching. Note that the I−V characteristics does not depend on the bias sweeping direction and no electroforming process is needed as indicated by Figure S2 in the Supporting Information. First-time switching of MIM structure reveals that pristine MIM structure is always in HRS, and the LRS is set by a positive bias (+8 V), whereas the MIM structure is reset to HRS by a negative bias (−8 V). It suggests that an as-prepared BFO-based MIM structure shows bipolar resistive switching behavior without an electroforming process.

To check the nonvolatility and reliability of the resistive switching in Au-BFO-Pt/Ti/Sapphire MIM structure, we performed pulse retention and endurance tests. The retention tests were carried out by first applying a writing bias pulse of +8 V or −8 V for 100 ms at room temperature to switch the MIM structures to LRS or HRS, respectively, and followed by detecting the resistance state with a small reading bias pulse of +2 V every 2 min at room temperature, 328 and 358 K, as shown in Figure 2a. The HRS is quite stable at room temperature, while the HRS at 328 and 358 K initially exhibits decreasing resistance (increase in the detected current) and becomes stable within 24 h. However, a degradation exists in all LRS tests. A stable LRS was obtained after around 5 h at room temperature and at 328 K, but the LRS at 358 K did not stabilize until around 40 h later. The stable LRS and HRS within the retention test time are more visible with the linear scale on the time axis (see Figure S3 in the Supporting Information). After 24 h, the resistance ratio R_{HRS}/R_{LRS} was around 100 at each test temperature. As indicated by the dashed lines in Figure 2a, the resistance ratio R_{HRS}/R_{LRS} can be well-kept after 10 years at room temperature, 328 and 358 K. The endurance tests were carried out at room temperature by repeating the set/read/reset/read process for more than 3 ×

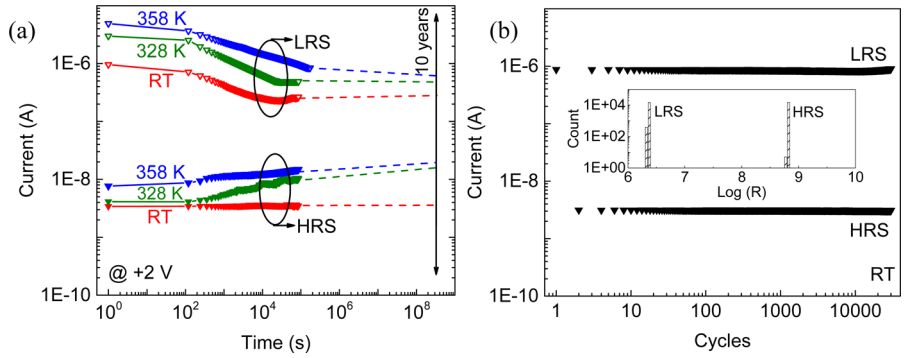

Figure 2. (a) Retention test results at room temperature (RT), 328 and 358 K. The extrapolated 10-year HRS/LRS retention time can be expressed by the dashed lines. (b) Endurance test result at RT. The inset in (b) indicates a statistics histograms of LRS/HRS. The LRS/HRS are set/reset by a writing bias of +8 V/−8 V with pulse length of 100 ms. The resistance states were read at +2 V.

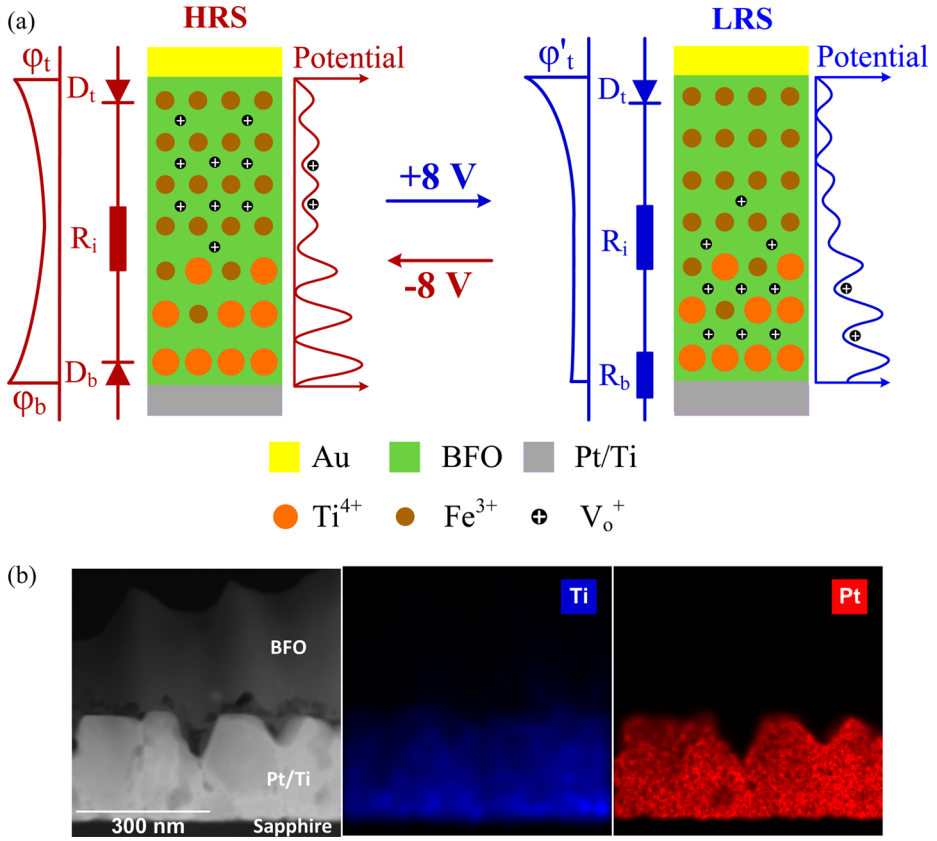

Figure 3. (a) Schematic presentation of the distribution of mobile V_o^+ (black circles) and fixed Ti^{4+} (orange circles) donors in the BFO thin film for HRS and LRS. The band diagrams of the Schottky barriers and the corresponding equivalent circuits are indicated in the left side of the schematic for each resistance state. Schematics of the potential profile for mobile V_o^+ donors are shown in the right side of the schematic for each resistance state. (b) Cross-section high-angle annular dark-field scanning transmission electron microscopy (HAADF-STEM) image and the energy-dispersive X-ray spectroscopy (EDX) mapping images of Ti (blue) and Pt (red) in BFO-Pt/Ti/Sapphire.

10^4 times. As shown in Figure 2b, highly stable LRS and HRS reading currents with the resistance ratio R_{HRS}/R_{LRS} more than 300 were recorded. The statistical data is given by the inset in Figure 2b, which indicates a narrow distribution of the resistance values in LRS and in HRS. The relative fluctuations (standard deviation divided by mean value) of LRS and HRS are 1.89% and 0.56%, respectively. However, the LRS and HRS reading currents of a reference sample of Au-BFO-Pt/Ti/SiO_2/Si MIM structure are fluctuant during the endurance test with the relative fluctuations of 12.27% and 19.42% for LRS and HRS, respectively, even though the *I*−*V* characteristic and retention test results of the reference sample are similar to that of Au-BFO-Pt/Ti/Sapphire MIM structure (see Figure S4 in the Supporting Information). The retention and endurance test results suggest that the bipolar resistive switching in Au-BFO-Pt/Ti/Sapphire MIM structure is nonvolatile and stable.

3.2. Resistive Switching Mechanism. As a gradually changing current is observed from the *I*−*V* characteristics, the mechanism of the resistive switching is interface-mediated instead of filament-related.[5,11] As shown in Figure 3a, the mechanism of the bipolar resistive switching observed in BFO thin films can be explained by the modification of the Schottky barrier at the BFO-Pt bottom interface by the drift of charged oxygen vacancies (V_o^+) under applied large electric fields during

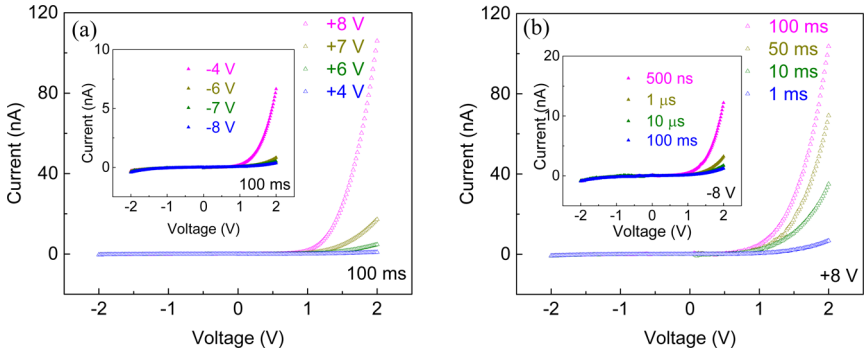

Figure 4. (a) *I*–*V* curves (ramped from −2 V to +2 V) measured after applying different magnitudes of writing bias with the pulse length of 100 ms; (b) *I*–*V* curves (ramped from −2 V to +2 V) measured after applying different lengths of writing bias with the magnitude of 8 V.

the writing step. Note that the bipolar resistive switching may also be caused by the electron trapping/detrapping[29] or by the ferroelectric switching.[12] However, these two possibilities can be excluded by the fact that the bipolar resistive switching from the electron trapping/detrapping mechanisms result in intrinsically low retention time,[29,30] and by the fact that the obvious ferroelectricity was not observed from the samples and the resistive switching can be tuned by the magnitude and length of the writing bias pulse which will be discussed later. As BFO can be considered as a n-type semiconductor due to the naturally formed V_o^+, a Schottky-like barrier is formed at the interface of Au-BFO and BFO-Pt.[31] The Ti diffusion from the Ti layer in the substrate causes the formation of a TiO_2 layer on the Pt surface,[32] which can be incorporated into the BFO film as in the case of $PbZrTiO_3$.[33] The Ti in BFO thin film was observed by the EDX mapping images as shown in Figure 3b. Note that there is no distinct resistive switching behavior in Au-BFO-Pt/Sapphire MIM structure without a Ti layer in the bottom electrode (see Figure S2 in the Supporting Information), which suggests that the Ti diffusing from the Pt/Ti bottom electrode plays a critical role on the resistive switching behaviors of BFO-based MIM structures. Compared to the V_o^+, it is more difficult for Ti^{4+} to migrate in perovskite materials due to the larger ionic radius of Ti^{4+} (0.68 nm) and the larger Ti migration energy.[34] Therefore, under moderate bias pulses, V_o^+ acts as mobile donor while Ti^{4+} acts as fixed donor in BFO. In the pristine state, the donors evenly distribute between the Au top electrode and Pt/Ti bottom electrode, and most of the fixed Ti^{4+} donors are accumulated near the BFO-Pt/Ti bottom interface because of a Ti diffusion from the Pt/Ti bottom electrode into BFO during the BFO growth at elevated temperature. As shown in Figure 3a, the equivalent circuit of HRS is a head-to-head rectifier which consists of two antiserially connected diodes (D_t and D_b) due to the Schottky-like contact (φ_t and φ_b) at both top (t) and bottom (b) interface and one resistor R_i denoting the bulk resistance of the BFO thin film. When a positive reading bias is applied, the current is blocked by the reversed bottom diode D_b, thus the MIM structure is in HRS. Due to the negative writing bias, the mobile V_o^+ donors drift toward the Au-BFO top interface, which sets up a small concentration gradient of donors. The resulting small concentration gradient of donors is stable at room temperature, while some of the mobile V_o^+ donors may diffuse toward the BFO-Pt bottom interface at 328 K and at 358 K due to the increasing diffusivity of the mobile V_o^+ donors with increasing temperature and the low potential barrier as indicated in Figure 3a. This diffusion mildly decreases the Schottky barrier height at the bottom interface (φ_b) and further increases the detected current. Therefore, a degradation of HRS was observed in the retention tests at 328 K and at 358 K. After applying a positive writing bias, most of the mobile V_o^+ donors drift toward the BFO-Pt bottom interface. The distribution of mobile V_o^+ donors is tunable by the defects in perovskite materials.[35,36] As shown in Figure 3a, close to the bottom interface several large potential barriers are formed on the atomic scale by the fixed Ti^{4+} donors. Once being drifted into the deep potential wells most of the mobile V_o^+ donors are trapped and can leave only the potential wells within an external electric field. The Schottky-like barrier at the BFO-Pt bottom interface is reduced resulting in an Ohmic contact (R_b), whereas the Schottky-like barrier at the Au-BFO top interface (φ_t') is increased because of the accumulation of donors at the bottom interface.[15,26] By applying a positive reading bias, the diode D_t' is forward biased and the MIM structure exhibits LRS. The increasing resistance of LRS observed in the retention tests may be due to the weak diffusion of mobile V_o^+ donors away from the BFO-Pt bottom interface which slightly increases the Schottky-like barrier at the bottom interface as there is a strong V_o^+ concentration gradient between top and bottom contact. After applying a negative writing bias, the mobile V_o^+ donors are released from the deep potential wells and drift toward the top electrode. Thus, the Schottky-like barrier at the BFO-Pt bottom interface is recovered and the MIM structure is reset to HRS.

Figure 3b shows the HAADF-STEM image and the EDX mapping images of Ti and Pt in BFO-Pt/Ti/Sapphire MIM structures. The Pt/Ti interface is not visible in the cross-section HAADF-STEM image due to the serious interdiffusion of Pt and Ti as indicated by the EDX mapping images. The cross-section HAADF-STEM image shows a rough BFO-Pt bottom interface in Au-BFO-Pt/Ti/Sapphire MIM structures; however, the BFO-Pt interface is smooth in the reference sample of Au-BFO-Pt/Ti/SiO_2/Si MIM structure (Figure S4 in the Supporting Information). With this rough BFO-Pt bottom interface, the local electric field is enhanced around the protrusions and directs the drift of mobile V_o^+ donors.[37,38] The randomness of the paths for the V_o^+ drift is reduced as in the case of ZnO resistive switching devices with Ag-nanoclusters.[38] Therefore, Au-BFO-Pt/Ti/Sapphire MIM structures with a rough BFO-Pt bottom interface possess much more stable endurance test results than the reference sample of Au-BFO-Pt/Ti/SiO_2/Si MIM structure with a smooth BFO-Pt bottom interface. This suggests that the development of structured

electrodes can solve the issue of nonuniformity for future ReRAM.[37,38]

It is difficult to directly and nondestructively characterize the physical changes responsible for the resistive switching, because the active regions of the devices are extremely small and buried under a metal contact.[26] In order to obtain further insight into the modification of the interface barrier by the redistribution of mobile V_o^+ donors, the $I-V$ curves in the small voltage range from −2 V to +2 V were measured after applying a writing bias pulse with different magnitude and length. Note that the MIM structure was fully reset to HRS by −8 V for 100 ms before applying every single positive writing bias pulse (+8, +7, +6, +4 V), whereas it was fully set to LRS by +8 V for 100 ms before applying every single negative writing bias pulse (−8, −7 −6, −4 V). Figure 4a shows the $I-V$ curves measured after applying a writing bias with the pulse length of 100 ms and with different amplitudes on Au-BFO-Pt/Ti/Sapphire MIM structure. It is clear that the current is small in both positive and negative voltage ranges when the MIM structure was fully reset to HRS (−8 V, 100 ms) which suggests a head-to-head rectifier behavior, whereas a forward rectification characteristic is observed when the MIM structure is fully set to LRS (+8 V, 100 ms), which suggests a forward rectifier behavior. This is in agreement with the equivalent circuits presented in Figure 3a. Under the assumption that the drift length of mobile V_o^+ is 600 nm with the writing bias of +8 V for 100 ms, the mobility of V_o^+ is calculated to be 4.5×10^{-9} cm^2 V^{-1} s^{-1} (drift length $L = vt$, drift velocity $v = \mu E$, where t, μ, and E denote the drift time, mobility and electric field, respectively), which is in the agreement with the reported mobility of V_o^+ in the range between 1×10^{-10} and 1×10^{-8} cm^2 V^{-1} s^{-1} in perovskite-type materials.[39−41] The behavior of the MIM structure as a forward rectifier or as a head-to-head rectifier becomes less pronounced with decreasing the magnitude of the writing bias. As the drift length of mobile V_o^+ decreases with decreasing electric fields, the MIM strture cannot be fully set/reset to LRS/HRS with a small writing bias. With the writing bias pulse length of 100 ms, the MIM structure cannot be set to LRS by the writing bias amplitude smaller than +7 V; however, the MIM structure cannot be reset to HRS by the writing bias amplitude below −4 V. The writing bias pulse length also influences the drift length of V_o^+. Figure 4b shows the $I-V$ curves measured after applying writing bias pulses of different length with the magnitude of 8 V. The head-to-head rectifier or forward rectifier behavior becomes less pronounced with decreasing length of the writing bias pulse. The MIM structure cannot be set to LRS with the writing bias pulse length smaller than 10 ms, whereas the MIM structure cannot be reset to HRS when the pulse length is smaller than 1 μs. It is easier to reset to HRS from LRS than to set to LRS from HRS, i.e., the HRS can be reset by the writing bias pulse with smaller magnitude and smaller length. This is because of the concentration gradient of V_o^+ in LRS and the asymmetric potential well introduced by Ti^{4+} as shown in Figure 3a (a larger potential barrier has to be overcome for the migration of mobile V_o^+ from top interface to bottom interface than for the migration from bottom interface to top interface). With large magnitude of the writing bias, a resistive switching device with fast speed can be realized, e.g. the MIM structure can be fully set/reset to LRS/HRS within 500 ns by a writing pulse magnitude of 20 V/−12 V (see Figure S5 in the Supporting Information), which further confirms that the resistive switching is not attributed to the ferroelectric switching. Note that the writing pulse length can be greatly reduced by a minor increase of the writing bias amplitude because the drift velocity of V_o^+ nonlinearly increases with increasing electric field,[42] which can be used to overcome the voltage−time dilemma.[29] By tuning the magnitude and length of the writing bias pulse, the resistive switching device can be continuously configured between the two fully switched LRS/HRS states for the multilevel nonvolatile memory applications.

In the following, we will discuss the variation of the Schottky barrier heights at top interface and at bottom interface in LRS and HRS. We expect that the Schottky barrier height at top interface in LRS (φ_t') is larger than the Schottky barrier height at top interface in HRS (φ_t) because of the different V_o^+ distribution in LRS and HRS (Figure 3a). Furthermore, due to the rather homogeneous distribution of V_o^+ in HRS, we expect that the Schottky barrier height at top interface in HRS (φ_t) is comparable to the Schottky barrier height at bottom interface in HRS (φ_b). The temperature-dependent $I-V$ characteristics (from −2 V to +2 V) were measured after the MIM structure was fully switched to HRS and LRS at room temperature (see Figure S6 in the Supporting Information). The current increases with the increasing temperature from 253 to 348 K. In HRS, the current is small in both the positive and negative bias range due to the Schottky-like barrier formed at both top and bottom interface, so the Schottky emission dominates the conduction. In the case of materials with low charge carriers' mobility, the $I-V$ characteristics can be described by the modified Richardson-Schottky equation:[43]

$$J = 2q\left(\frac{2\pi m_{\text{eff}} kT}{h^2}\right)^{3/2} \mu E \exp\left(-\frac{q}{kT}\left(\varphi - \sqrt{\frac{qE}{4\pi\varepsilon_0\varepsilon_r}}\right)\right) \quad (1)$$

where J is the current density, E is the electric field, m_{eff} is the effective mass, μ is the electron mobility, φ is the potential barrier at zero bias, ε_r is the dielectric constant, and the other symbols have their usual meaning. According to eq 1, the Schottky-Simmons graphic representation can be obtained at a constant voltage as follows

$$\ln\left(\frac{J}{T^{3/2}}\right) = \ln\left(2q\left(\frac{2\pi m_{\text{eff}} kT}{h^2}\right)^{3/2} \mu E\right) - \frac{q}{kT}\left(\varphi - \sqrt{\frac{qE}{4\pi\varepsilon_0\varepsilon_r}}\right) \quad (2)$$

The representation $\ln(J/T^{3/2}) \sim 1/T$ should give a straight line, and the apparent potential barrier for the respective constant voltage can be estimated from the slope. Figure 5a,b show the $\ln(J/T^{3/2}) \sim 1000/T$ plot together with the linear fitting in negative and positive bias range, respectively. Further on, representing the obtained apparent potential barrier value (φ_t in inset of Figure 5a and φ_b in inset of Figure 5b) as a function of $V^{1/2}$, the potential barrier at zero bias (φ_{t0} and φ_{t0}) can be extracted from the intercept at φ_t and φ_b axes. In HRS, the current is blocked by the Schottky-like barrier at top interface (φ_t) in negative bias range, while the current is blocked by the Schottky-like barrier at bottom interface (φ_b) in positive bias range. Therefore, the zero bias Schottky barrier height in HRS at top and bottom interface (φ_{t0} and φ_{b0}) can be extracted from the plot in negative and positive bias range, respectively, which are deduced to be 0.16 eV (φ_{t0}) and 0.13 eV (φ_{b0}), respectively.

In LRS, the current is mainly dominated by the Schottky-like barrier at top interface. As shown in Figure 5c, the temperature dependent zero bias Schottky barrier height and ideality factor

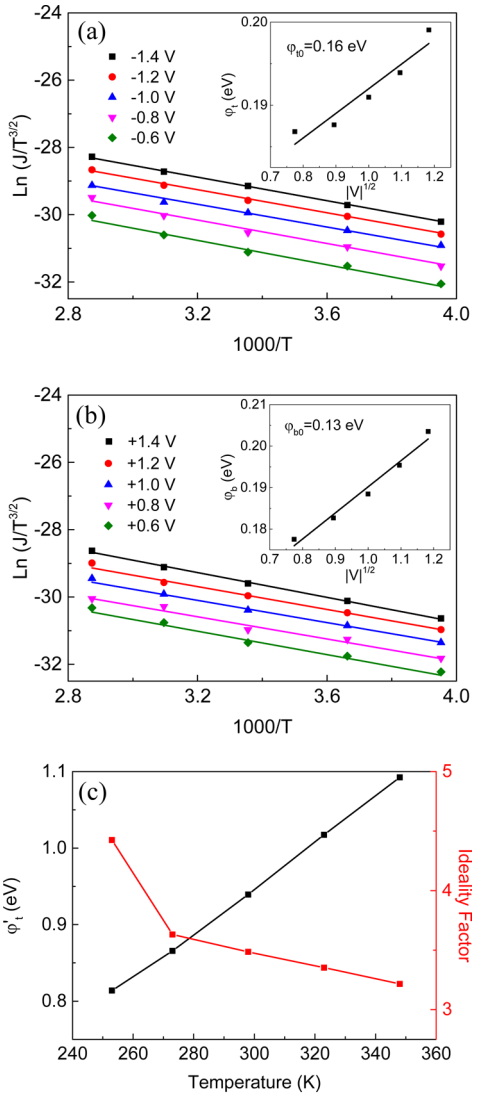

Figure 5. Schottky–Simmons representation of the (a) negative bias range and (b) positive bias range for HRS. The insets indicate the zero bias Schottky barrier heights formed on top (φ_{t0}) and bottom (φ_{b0}) interface in Au-BFO-Pt/Ti/Sapphire MIM structure. (c) Temperature-dependent zero bias Schottky barrier height and ideality factor for LRS in Au-BFO-Pt/Ti/Sapphire.

can be fitted from the temperature dependent $I-V$ curves by using the Shockley equation[44] as follows

$$I = AA*T^2\exp\left(-\frac{q\varphi_0}{kT}\right)\left\{\exp\left[\frac{q(V - IR_s)}{nkT}\right] - 1\right\} + \frac{(V - IR_s)}{R_p} \quad (3)$$

where A is the area of the diodes, A^* is the effective Richardson constant, φ_0 is the zero bias barrier height, R_s is the series resistance, R_p is the parallel resistance, n is the ideality factor, and the other symbols have their usual meaning. With the increasing temperature from 253 to 348 K, the ideality factor decreases from 4.42 to 3.22 and the zero bias Schottky barrier height in LRS at top interface (φ_{t0}') increases from 0.81 to 1.09 eV. This suggests that the zero bias Schottky barrier height at top interface is greatly increased when the MIM structure is set to LRS with V_o^+ drifting toward the bottom interface. The relatively large ideality factor indicates the deviation of $I-V$ characteristics from thermionic emission theory. This may be due to the large series resistance in the order of megaohm and the lateral inhomogeneity of the Schottky barrier height, which becomes more pronounced as the temperature decreases. Because electrons possess a small kinetic energy at low temperature, they prefer to pass through the lowest barrier.

3.3. Local Resistive Switching. The lateral inhomogeneity of the Schottky barrier height is evidenced by conductive AFM measurements shown in Figure 6. The AFM topography of the as-grown BFO thin film with a scanning size of 2 × 2 μm^2 is shown in Figure 6a, which indicates a surface roughness of 12.5 nm. Figure 6b shows the local $I-V$ characteristics which were measured by putting the top conductive tip on the surface of BFO thin film. An obvious resistive switching is observed in the negative bias range. Note that the bias polarity is opposite to the $I-V$ measurements shown in Figure 1, because the voltage bias is applied on the Pt bottom electrode as indicated by the inset in Figure 6b. The size of the top conductive tip is 20 nm. The local area with the size of 2 × 2 μm^2 can be switched to LRS or HRS by scanning the conductive tip with a voltage bias of −10 V or +10 V on the Pt bottom electrode (see Figure S7 in the Supporting Information). Figure 6c, d show the current images in LRS and HRS, respectively. The reading bias was −4 V, as the difference between LRS and HRS is not visible in linear scale until −4 V in the local $I-V$ characteristic as shown in Figure 6b. In HRS, only some small leakage current is observed, while in LRS some conductive areas appear in some grains. The local resistive switching suggests the possibility to scale down the resistive switching cell to the grain size. The grain size is a function of film thickness and thermal budget of the deposition and post processing. Lateral and vertical dimensions have to be scaled and thermal treatments have to be tuned accordingly. Recently, it was shown that excellent switching data can be achieved for scaled electrodes and significantly reduced film thickness.[45] Even though Figure 6c, d show the inhomogeneous distribution of the current, the resistive switching does not come from the formation and rupture of filaments as discussed in section 3.2, it indicates the lateral inhomogeneity of the Schottky barrier height and the conductive shunts formed by the defects existing in the BFO bulk.[46,47] Possibly, a larger writing voltage is required to switch the highly resistive locations with high Schottky barrier height or without the conductive shunts.

4. CONCLUSIONS

In summary, polycrystalline BFO thin films on Pt/Ti/Sapphire have been prepared by the PLD process and show excellent nonvolatile bipolar resistive switching behavior. Both mobile and fixed donors contribute to the nonvolatile bipolar resistive switching, i.e., the trapping and detrapping of mobile V_o^+ donors by the fixed Ti^{4+} donors under the writing bias changes the Schottky barrier heights at top and bottom interface. The resistive switching can be continuously configured by tuning the amplitude and length of the writing bias pulse, which makes it possible to realize the multilevel resistive switching and to increase the switching speed. The local resistive switching suggests the possibility to scale down the resistive switching cell to the grain size.

dx.doi.org/10.1021/am504871g | ACS Appl. Mater. Interfaces 2014, 6, 19758–19765

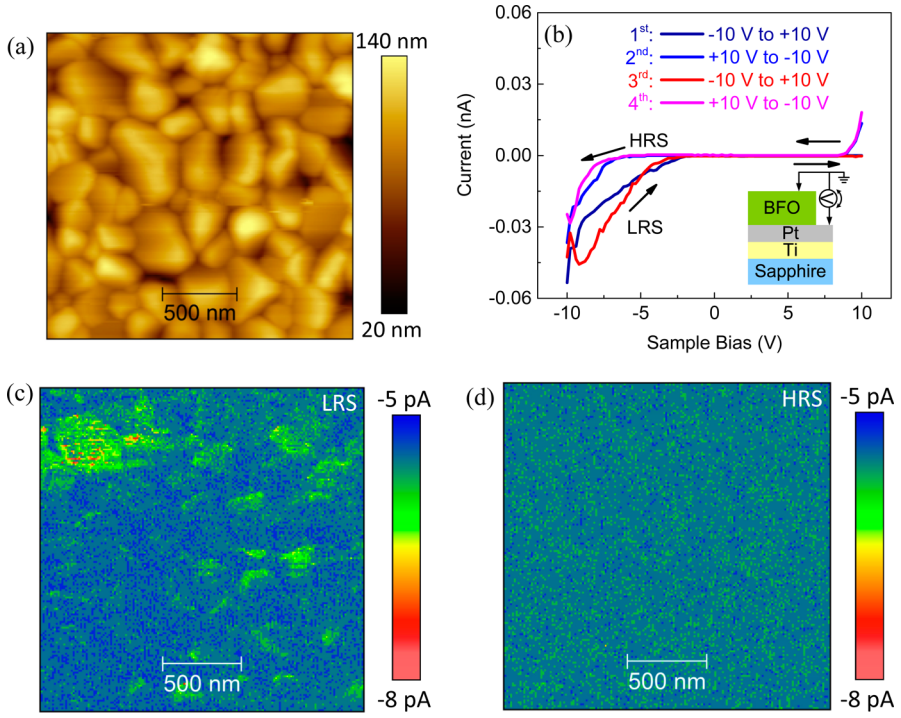

Figure 6. (a) AFM topography image of as-prepared BFO thin film with a scanned size of 2 × 2 μm^2. The inset in b shows the schematic of the conductive AFM measurements on BFO-Pt/Ti/Sapphire. The voltage is applied on the Pt bottom electrode, and the top conductive tip is grounded, which is opposite to the *I*−*V* measurements shown in Figure 1. (b) Local *I*−*V* characteristics measured with the conductive tip on the surface of BFO thin film. The current images measured from (c) LRS and (d) HRS with a reading bias of −4 V applied on the Pt bottom electrode.

■ ASSOCIATED CONTENT

Supporting Information

GIXRD pattern, additional *I*−*V* characteristics and CSAFM current images of Au-BFO-Pt/Ti/Sapphire MIM structure; electric characterizations of Au-BFO-Pt/Sapphire and Au-BFO-Pt/Ti/SiO_2/Si MIM structures. This material is available free of charge via the Internet at http://pubs.acs.org.

■ AUTHOR INFORMATION

Corresponding Authors

*E-mail: tiangui.you@s2012.tu-chemnitz.de.

*E-mail: heidemarie.schmidt@etit.tu-chemnitz.de. Tel: +49 (0) 371 531 32481. Fax: +49 (0)371 531-832481.

Notes

The authors declare no competing financial interest.

■ ACKNOWLEDGMENTS

T. You acknowledges the China Scholarship Council (Grant Code: 201206970006) and the Initiative and Networking Fund of the Helmholtz Association (Grant Code: VI MEMRIOX VH-VI-422), D. Bürger, A. Beyer, K. Volz, and H. Schmidt acknowledge the Deutsche Forschungsgemeinschaft (Grant Code: BU 2956/1-1, VO 805/2, and SCHM 1663/4-1).

■ REFERENCES

(1) Vogel, E. Technology and Metrology of New Electronic Materials and Devices. *Nat. Nanotechnol.* **2007**, *2*, 25−32.

(2) Xia, Q.; Robinett, W.; Cumbie, M. W.; Banerjee, N.; Cardinali, T. J.; Yang, J. J.; Wu, W.; Li, X.; Tong, W. M.; Strukov, D. B. Memristor−CMOS Hybrid Integrated Circuits for Reconfigurable Logic. *Nano Lett.* **2009**, *9*, 3640−3645.

(3) Waser, R.; Aono, M. Nanoionics-based Resistive Switching Memories. *Nat. Mater.* **2007**, *6*, 833−840.

(4) Lee, M.-J.; Lee, C. B.; Lee, D.; Lee, S. R.; Chang, M.; Hur, J. H.; Kim, Y.-B.; Kim, C.-J.; Seo, D. H.; Seo, S. A Fast, High-endurance and Scalable Non-volatile Memory Device Made from Asymmetric Ta_2O_{5-x}/TaO_{2-x} Bilayer Structures. *Nat. Mater.* **2011**, *10*, 625−630.

(5) Borghetti, J.; Snider, G. S.; Kuekes, P. J.; Yang, J. J.; Stewart, D. R.; Williams, R. S. 'Memristive' Switches Enable 'Stateful' Logic Operations via Material Implication. *Nature* **2010**, *464*, 873−876.

(6) Linn, E.; Rosezin, R.; Tappertzhofen, S.; Böttger, U.; Waser, R. Beyond von Neumann-Logic Operations in Passive Crossbar Arrays Alongside Memory Operations. *Nanotechnology* **2012**, *23*, 305205.

(7) Jo, S. H.; Chang, T.; Ebong, I.; Bhadviya, B. B.; Mazumder, P.; Lu, W. Nanoscale Memristor Device as Synapse in Neuromorphic Systems. *Nano Lett.* **2010**, *10*, 1297−1301.

(8) You, T.; Shuai, Y.; Luo, W.; Du, N.; Bürger, D.; Skorupa, I.; Hübner, R.; Henker, S.; Mayr, C.; Schüffny, R.; Mikolajick, T.; Schmidt, O. G.; Schmidt, H. Exploiting Memristive $BiFeO_3$ Bilayer Structures for Compact Sequential Logics. *Adv. Funct. Mater.* **2014**, *24*, 3357−3365.

(9) Du, N.; Manjunath, N.; Shuai, Y.; Bürger, D.; Skorupa, I.; Schüffny, R.; Mayr, C.; Basov, D. N.; Di Ventra, M.; Schmidt, O. G.; Schmidt, H. Novel Implementation of Memristive Systems for Data Encryption and Obfuscation. *J. Appl. Phys.* **2014**, *115*, 124501.

(10) Chae, S. C.; Lee, J. S.; Kim, S.; Lee, S. B.; Chang, S. H.; Liu, C.; Kahng, B.; Shin, H.; Kim, D. W.; Jung, C. U. Random Circuit Breaker Network Model for Unipolar Resistance Switching. *Adv. Mater.* **2008**, *20*, 1154−1159.

(11) Kwon, D.-H.; Kim, K. M.; Jang, J. H.; Jeon, J. M.; Lee, M. H.; Kim, G. H.; Li, X.-S.; Park, G.-S.; Lee, B.; Han, S. Atomic Structure of Conducting Nanofilaments in TiO_2 Resistive Switching Memory. *Nat. Nanotechnol.* **2010**, *5*, 148−153.

(12) Jiang, A. Q.; Wang, C.; Jin, K. J.; Liu, X. B.; Scott, J. F.; Hwang, C. S.; Tang, T. A.; Lu, H. B.; Yang, G. Z. A Resistive Memory in Semiconducting $BiFeO_3$ Thin-Film Capacitors. *Adv. Mater.* **2011**, *23*, 1277−1281.

(13) Xu, Z.; Jin, K.; Gu, L.; Jin, Y.; Ge, C.; Wang, C.; Guo, H.; Lu, H.; Zhao, R.; Yang, G. Evidence for a Crucial Role Played by Oxygen

Vacancies in $LaMnO_3$ Resistive Switching Memories. *Small* **2012**, *8*, 1279−1284.
(14) Kim, T. W.; Zeigler, D. F.; Acton, O.; Yip, H. L.; Ma, H.; Jen, A. K. Y. All-Organic Photopatterned One Diode-One Resistor Cell Array for Advanced Organic Nonvolatile Memory Applications. *Adv. Mater.* **2012**, *24*, 828−833.
(15) Yang, J. J.; Borghetti, J.; Murphy, D.; Stewart, D. R.; Williams, R. S. A Family of Electronically Reconfigurable Nanodevices. *Adv. Mater.* **2009**, *21*, 3754−3758.
(16) Guo, Y.; Guo, B.; Dong, W.; Li, H.; Liu, H. Evidence for Oxygen Vacancy or Ferroelectric Polarization Induced Switchable Diode and Photovoltaic Effects in $BiFeO_3$ Based Thin Films. *Nanotechnology* **2013**, *24*, 275201.
(17) Rozenberg, M.; Inoue, I.; Sanchez, M. Nonvolatile Memory with Multilevel Switching: A Basic Model. *Phys. Rev. Lett.* **2004**, *92*, 178302.
(18) Choi, T.; Lee, S.; Choi, Y.; Kiryukhin, V.; Cheong, S.-W. Switchable Ferroelectric Diode and Photovoltaic Effect in $BiFeO_3$. *Science* **2009**, *324*, 63−66.
(19) Kim, W.-H.; Son, J. Y.; Jang, H. M. Confinement of Ferroelectric Domain-Wall Motion at Artificially Formed Conducting-Nanofilaments in Epitaxial $BiFeO_3$ Thin Films. *ACS Appl. Mater. Interfaces* **2014**, *6*, 6346−6350.
(20) Hong, S.; Choi, T.; Jeon, J. H.; Kim, Y.; Lee, H.; Joo, H. Y.; Hwang, I.; Kim, J. S.; Kang, S. O.; Kalinin, S. V. Large Resistive Switching in Ferroelectric $BiFeO_3$ Nano-Island Based Switchable Diodes. *Adv. Mater.* **2013**, *25*, 2339−2343.
(21) Rana, A.; Lu, H.; Bogle, K.; Zhang, Q.; Vasudevan, R.; Thakare, V.; Gruverman, A.; Ogale, S.; Valanoor, N. Scaling Behavior of Resistive Switching in Epitaxial Bismuth Ferrite Heterostructures. *Adv. Funct. Mater.* **2014**, *24*, 3962−3969.
(22) Tsurumaki, A.; Yamada, H.; Sawa, A. Impact of Bi Deficiencies on Ferroelectric Resistive Switching Characteristics Observed at p-Type Schottky-Like Pt/$Bi_{1-\delta}FeO_3$ Interfaces. *Adv. Funct. Mater.* **2012**, *22*, 1040−1047.
(23) Yin, K.; Li, M.; Liu, Y.; He, C.; Zhuge, F.; Chen, B.; Lu, W.; Pan, X.; Li, R.-W. Resistance Switching in Polycrystalline $BiFeO_3$ Thin Films. *Appl. Phys. Lett.* **2010**, *97*, 042101.
(24) Shen, W.; Bell, A.; Karimi, S.; Reaney, I. M. Local Resistive Switching of Nd Doped $BiFeO_3$ Thin Films. *Appl. Phys. Lett.* **2012**, *100*, 133505.
(25) Wu, L.; Jiang, C.; Xue, D. Resistive Switching in Doped $BiFeO_3$ Films. *J. Appl. Phys.* **2014**, *115*, 17D716.
(26) Yang, J. J.; Pickett, M. D.; Li, X.; Ohlberg, D. A.; Stewart, D. R.; Williams, R. S. Memristive Switching Mechanism for Metal/Oxide/Metal Nanodevices. *Nat. Nanotechnol.* **2008**, *3*, 429−433.
(27) Sawa, A. Resistive Switching in Transition Metal Oxides. *Mater. Today* **2008**, *11*, 28−36.
(28) Yang, Y.; Lu, W. Nanoscale Resistive Switching Devices: Mechanisms and Modeling. *Nanoscale* **2013**, *5*, 10076−10092.
(29) Schroeder, H.; Zhirnov, V. V.; Cavin, R. K.; Waser, R. Voltage-Time Dilemma of Pure Electronic Mechanisms in Resistive Switching Memory cells. *J. Appl. Phys.* **2010**, *107*, 054517.
(30) Shibuya, K.; Dittmann, R.; Mi, S.; Waser, R. Impact of Defect Distribution on Resistive Switching Characteristics of Sr_2TiO_4 Thin Films. *Adv. Mater.* **2010**, *22*, 411−414.
(31) Ge, C.; Jin, K.-J.; Wang, C.; Lu, H.-B.; Wang, C.; Yang, G.-Z. Numerical Investigation into the Switchable Diode Effect in Metal-Ferroelectric-Metal Structures. *Appl. Phys. Lett.* **2011**, *99*, 063509.
(32) Sreenivas, K.; Reaney, I.; Maeder, T.; Setter, N.; Jagadish, C.; Elliman, R. Investigation of Pt/Ti Bilayer Metallization on Silicon for Ferroelectric Thin Film Integration. *J. Appl. Phys.* **1994**, *75*, 232−239.
(33) Maeder, T.; Muralt, P.; Sagalowicz, L.; Setter, N. In-Situ Sputter Deposition of PT and PZT Films on Platinum and RuO_2 Electrodes. *Microelectron. Eng.* **1995**, *29*, 177−180.
(34) Mizoguchi, T.; Takahashi, N.; Lee, H.-S. First-Principles Study on Migration Mechanism in $SrTiO_3$. *Appl. Phys. Lett.* **2011**, *98*, 091909.
(35) Kimmel, A. V.; Weaver, P. M.; Cain, M. G.; Sushko, P. V. Defect-Mediated Lattice Relaxation and Domain Stability in Ferroelectric Oxides. *Phys. Rev. Lett.* **2012**, *109*, 117601.
(36) Yang, Q.; Cao, J. X.; Ma, Y.; Zhou, Y. C.; Jiang, L. M.; Zhong, X. L. Strain Effects on Formation and Migration Energies of Oxygen Vacancy in Perovskite Ferroelectrics: A First-Principles Study. *J. Appl. Phys.* **2013**, *113*, 184110.
(37) Yoon, J. H.; Han, J. H.; Jung, J. S.; Jeon, W.; Kim, G. H.; Song, S. J.; Seok, J. Y.; Yoon, K. J.; Lee, M. H.; Hwang, C. S. Highly Improved Uniformity in the Resistive Switching Parameters of TiO_2 Thin Films by Inserting Ru Nanodots. *Adv. Mater.* **2013**, *25*, 1987−1992.
(38) Wang, Z.; Xu, H.; Zhang, L.; Li, X.; Ma, J.; Zhang, X.; Liu, Y. Performance Improvement of Resistive Switching Memory Achieved by Enhancing Local-Electric-Field Near Electromigrated Ag-nanoclusters. *Nanoscale* **2013**, *5*, 4490−4494.
(39) Blanc, J.; Staebler, D. L. Electrocoloration in $SrTiO_3$: Vacancy Drift and Oxidation-Reduction of Transition Metals. *Phys. Rev. B* **1971**, *4*, 3548.
(40) El Kamel, F.; Gonon, P.; Ortega, L.; Jomni, F.; Yangui, B. Space Charge Limited Transient Currents and Oxygen Vacancy Mobility in Amorphous $BaTiO_3$ Thin Films. *J. Appl. Phys.* **2006**, *99*, 094107.
(41) Waser, R. Bulk Conductivity and Defect Chemistry of Acceptor-Doped Strontium Titanate in the Quenched State. *J. Am. Ceram. Soc.* **1991**, *74*, 1934−1940.
(42) Strukov, D. B.; Williams, R. S. Exponential Ionic Drift: Fast Switching and Low Volatility of Thin-Film Memristors. *Appl. Phys. A Mater.Sci. Process.* **2009**, *94*, 515−519.
(43) Simmons, J. Richardson-Schottky Effect in Solids. *Phys. Rev. Lett.* **1965**, *15*, 967.
(44) Dimoulas, A.; Tsipas, P.; Sotiropoulos, A.; Evangelou, E. Fermi-Level Pinning and Charge Neutrality Level in Germanium. *Appl. Phys. Lett.* **2006**, *89*, 252110.
(45) Jin, L.; Shuai, Y.; Ou, X.; Siles, P. F.; Zeng, H. Z.; You, T.; Du, N.; Bürger, D.; Skorupa, I.; Zhou, S.; Luo, W. B.; Wu, C. G.; Zhang, W. L.; Mikolajick, T.; Schmidt, O. G.; Schmidt, H. Resistive Switching in Unstructured, Polycrystalline $BiFeO_3$ Thin Films with Downscaled Electrodes. *Phys. Status. Solidi A* **2014**, DOI: 10.1002/pssa.201431298.
(46) Ou, X.; Shuai, Y.; Luo, W.; Siles, P. F.; Kögler, R.; Fiedler, J.; Reuther, H.; Zhou, S.; Hübner, R.; Facsko, S.; Helm, M.; Mikolajick, T.; Schmidt, O. G.; Schmidt, H. Forming-Free Resistive Switching in Multiferroic $BiFeO_3$ Thin Films with Enhanced Nanoscale Shunts. *ACS Appl. Mater. Interfaces* **2013**, *5*, 12764−12771.
(47) Bersuker, G.; Gilmer, D. C.; Veksler, D.; Kirsch, P.; Vandelli, L.; Padovani, A.; Larcher, L.; McKenna, K.; Shluger, A.; Iglesias, V.; Porti, M.; Naffria, M. Metal Oxide Resistive Memory Switching Mechanism Based on Conductive Filament Properties. *J. Appl. Phys.* **2011**, *110*, 124518.